

Clarifying the relationship between redox activity and electrochemical stability in solid electrolytes

Schwietert, Tammo K.; Arszewska, Violetta A.; Wang, Chao; Yu, Chuang; Vasileiadis, Alexandros; de Klerk, Niek J.J.; Hageman, Jart; Xu, Yaolin; van der Maas, Eveline; Kelder, Erik M.

DOI

[10.1038/s41563-019-0576-0](https://doi.org/10.1038/s41563-019-0576-0)

Publication date

2020

Document Version

Final published version

Published in

Nature Materials

Citation (APA)

Schwietert, T. K., Arszewska, V. A., Wang, C., Yu, C., Vasileiadis, A., de Klerk, N. J. J., Hageman, J., Xu, Y., van der Maas, E., Kelder, E. M., Ganapathy, S., Wagemaker, M., & More Authors (2020). Clarifying the relationship between redox activity and electrochemical stability in solid electrolytes. *Nature Materials*, 19(4), 428-435. <https://doi.org/10.1038/s41563-019-0576-0>

Important note

To cite this publication, please use the final published version (if applicable).
Please check the document version above.

Copyright

Other than for strictly personal use, it is not permitted to download, forward or distribute the text or part of it, without the consent of the author(s) and/or copyright holder(s), unless the work is under an open content license such as Creative Commons.

Takedown policy

Please contact us and provide details if you believe this document breaches copyrights.
We will remove access to the work immediately and investigate your claim.

Clarifying the relationship between redox activity and electrochemical stability in solid electrolytes

Tammo K. Schwietert^{1,3}, Violetta A. Arszewska^{1,3}, Chao Wang¹, Chuang Yu¹, Alexandros Vasileiadis¹, Niek J. J. de Klerk¹, Jart Hageman¹, Thomas Hupfer², Ingo Kerkamm², Yaolin Xu¹, Eveline van der Maas¹, Erik M. Kelder¹, Swapna Ganapathy^{1*} and Marnix Wagemaker^{1*}

All-solid-state Li-ion batteries promise safer electrochemical energy storage with larger volumetric and gravimetric energy densities. A major concern is the limited electrochemical stability of solid electrolytes and related detrimental electrochemical reactions, especially because of our restricted understanding. Here we demonstrate for the argyrodite-, garnet- and NASICON-type solid electrolytes that the favourable decomposition pathway is indirect rather than direct, via (de)lithiated states of the solid electrolyte, into the thermodynamically stable decomposition products. The consequence is that the electrochemical stability window of the solid electrolyte is notably larger than predicted for direct decomposition, rationalizing the observed stability window. The observed argyrodite metastable (de)lithiated solid electrolyte phases contribute to the (ir)reversible cycling capacity of all-solid-state batteries, in addition to the contribution of the decomposition products, comprehensively explaining solid electrolyte redox activity. The fundamental nature of the proposed mechanism suggests this is a key aspect for solid electrolytes in general, guiding interface and material design for all-solid-state batteries.

All-solid-state-batteries (ASSBs) are attracting ever increasing attention due to their high intrinsic safety, achieved by replacing the flammable and reactive liquid electrolyte by a solid electrolyte¹. In addition, a higher energy density in ASSBs may be achieved through (a) bipolar stacking of the electrodes, which reduces the weight of the non-active battery parts and (b) by potentially enabling the use of a Li-metal anode, which possesses the maximum theoretical Li capacity and lowest electrochemical potential (3,860 mAh g⁻¹ and -3.04 V versus the standard hydrogen electrode). The success of ASSBs relies first on solid electrolytes, with a high Li-ion conductivity²⁻⁵. A second prerequisite is the electrochemical stability at the interfaces of the solid electrolyte with the electrode material in the range of their working potential. Any electrochemical decomposition of the solid electrolyte may lead to decomposition products with poor ionic conductivity that increase the internal battery resistance^{2-4,6}. Third, ASSBs require mechanical stability, as the changes in volume of the electrode materials on (de)lithiation, as well as decomposition reactions at the electrode-electrolyte interface may lead to contact loss, also increasing the internal resistance and lowering the capacity^{2-4,7}.

Initially, for many solid electrolytes wide electrochemical stability windows were reported^{4,8-11}, which appeared in practice to be much more limited^{4,12,13}. Evaluation of the electrochemical stability, based on differences in formation energies, indeed lead to much narrower stability windows^{14,15}; however, practical stability windows typically appeared wider^{4,12,13}. As a thermodynamic evaluation does not take into account kinetic barriers for decomposition reactions, which should be expected to play a critical role¹³, the mechanisms of solid electrolyte decomposition are poorly understood, presenting one of the major challenges for ASSBs^{2-4,7,12,13}. Another important aspect, directly related to this, is the potentially significant contribution of the typically Li-rich solid electrolytes through (de)lithiation

reactions, either directly or indirectly¹⁶. In general, redox activity can be expected near the interface between the solid electrolyte and the electronically conductive components of the electrode (electrode active material and carbon additives¹⁷), but may also extend deep into the solid electrolyte through short-range electron conductivity of the electrolyte itself¹⁸. Understanding the redox activity of solid electrolytes, and its correlation with the electrochemical stability window, is thus of fundamental importance for the development of stable solid-solid interfaces in ASSBs.

Here, we demonstrate that the electrochemical stability window of the argyrodite Li₆PS₅Cl (LPSC) solid electrolyte is determined by the solid electrolyte redox activity, that is, lithiation, on reduction of phosphorus and delithiation on oxidation of sulfur, before decomposing into more stable products. As demonstrated by density functional theory (DFT) simulations, this kinetically favourable indirect decomposition pathway effectively widens the electrochemical stability window, compared to direct decomposition into stable products, in excellent agreement with accurate electrochemical measurements. The (de)lithiated argyrodite phases are directly observed with X-ray diffraction (XRD) and solid-state NMR, providing direct evidence of this indirect decomposition mechanism. As solid electrolytes are designed to provide fast ionic conduction, the indirect decomposition through (de)lithiation is proposed to be relevant for solid electrolytes in general, determining the practical electrochemical stability window. This is further supported by the agreement between the measured and the predicted indirect decomposition mechanism for Li₇La₃Zr₂O₁₂ (LLZO) garnet-type and Li_{1.5}Al_{0.5}Ge_{1.5}(PO₄)₃ (LAGP) NASICON-type solid electrolytes. This mechanism establishes that not only the decomposition products but also the solid electrolyte structure itself contribute to the reversible capacity in ASSBs, making the present findings highly relevant for the working and development of ASSBs.

¹Storage of Electrochemical Energy, Faculty of Radiation Science and Technology, Delft University of Technology, Delft, the Netherlands. ²Robert Bosch GmbH, Corporate Sector Research and Advance Engineering, Renningen, Germany. ³These authors contributed equally: Tammo K. Schwietert, Violetta A. Arszewska. *e-mail: s.ganapathy@tudelft.nl; m.wagemaker@tudelft.nl

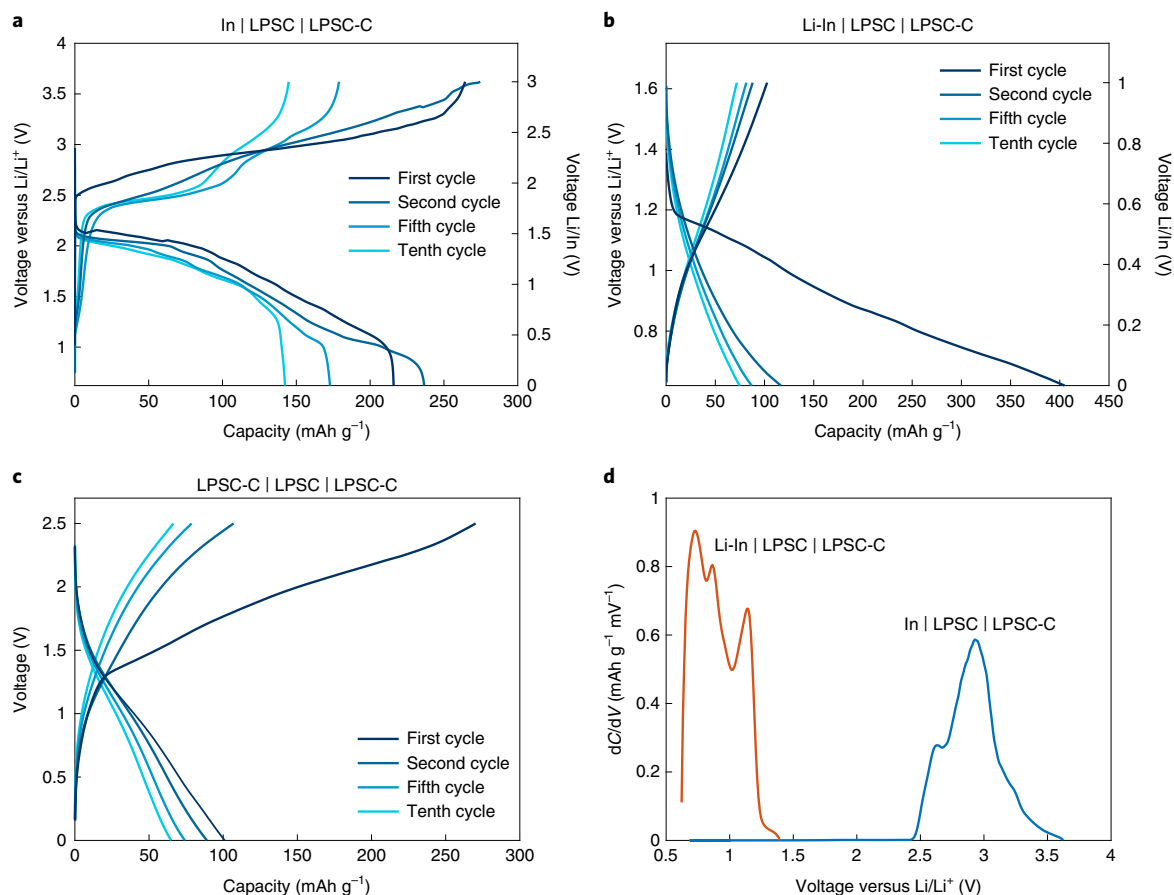


Fig. 1 | Voltage profiles and differential capacity curve of the LPSC-C electrode. a–c, Voltage profile of the first, second, fifth and tenth cycles of: In|LPSC|LPSC-C ASSB starting from charge and on galvanostatic oxidation, where the LPSC-C electrode shows a voltage plateau at 2.5 V, reaching a total charge capacity of 264 mAh g_{LPSC}⁻¹ when charged to 3.63 V (**a**); Li-In|LPSC|LPSC-C ASSB starting from discharge and on galvanostatic reduction, where the LPSC-C electrode shows a voltage plateau at around 1.2 V, with a discharge capacity of 405 mAh g_{LPSC}⁻¹ when discharged to 0.63 V (**b**); and LPSC-C|LPSC|LPSC-C, a one-material (LPSC) ASSB, shows an initial charge capacity of 270 mAh g_{LPSC}⁻¹, which drops to 107 mAh g_{LPSC}⁻¹ in the second cycle (**c**). **d,** The differential capacity dC/dV curve of the In|LPSC|LPSC-C (blue) and the Li-In|LPSC|LPSC-C battery (orange) showing the first oxidation and first reduction of LPSC. Electrochemical activity is observed below 1.25 V and above 2.50 V versus Li/Li⁺, indicating an electrochemical stability window of 1.25 V. Note that these experiments should be expected to approach thermodynamic conditions, and hence the contribution of overpotentials is minimal. This is because the applied current density (see Methods) is distributed over the very large interface area between the conductive carbon additives and the solid electrolyte (>1 m²).

Electrochemical activity of the argyrodite LPSC

The electrochemical stability, especially for thiophosphate solid electrolytes, was shown to be significantly lower than initially expected^{10,17,19–22}, where the consequential decomposition reactions have had a large impact on the ASSB performance^{11,21–25}. To investigate the electrochemical stability and the role of electrochemical reactions in solid electrolytes, the argyrodite LPSC, introduced by Deiseroth et al.²⁶, is employed both as active material and solid electrolyte in ASSBs. To induce oxidation and reduction reactions of the solid electrolyte, carbon black and carbon nanofibres are mixed in with the LPSC. The mixture is referred to as the LPSC-C electrode (for details see Methods). To study the oxidation and reduction independently, while at the same time preventing the redox activity of the decomposition products from interfering with the decomposition itself, individual cells are prepared for the first oxidation and for the first reduction. An In|LPSC|LPSC-C battery is cycled galvanostatically starting with oxidation, and a Li-In|LPSC|LPSC-C battery starting with reduction, the resulting voltage curves of which are shown in Fig. 1a,b. Unless otherwise specified, all voltages are expressed versus the Li/Li⁺ potential. The large partially reversible

specific capacities demonstrate that LPSC can undergo severe oxidation and reduction reactions, and the low coulombic efficiencies of 70% and 40% on first oxidation and reduction, respectively, suggest the formation of a significant number of decomposition products. The decreasing capacity of the initial cycles (Supplementary Fig. 1) indicates that these decomposition reactions increase the impedance. However, on extended cycling, the reversible capacity remains relatively constant, which could indicate that the decomposition products are able to deliver reversible electrochemical activity, as already suggested for LPSC by Auvergnot et al.²⁷ and worked out in detail by Tan et al.²⁵. Since LPSC can undergo both oxidation and reduction reactions, it can be used to assemble a one-material battery, similar to what was reported for the Li₁₀GeP₂S₁₂ solid electrolyte, for which the combination of decomposition products at the cathode and anode provided the reversible redox¹⁶. During the first charge, the activity appears to set in at around 1.25 V, which is a direct indication of the practical electrochemical stability window. To evaluate the practical electrochemical stability window more accurately, the differential capacity is determined from the first charge of the In|LPSC|LPSC-C battery and from the first discharge

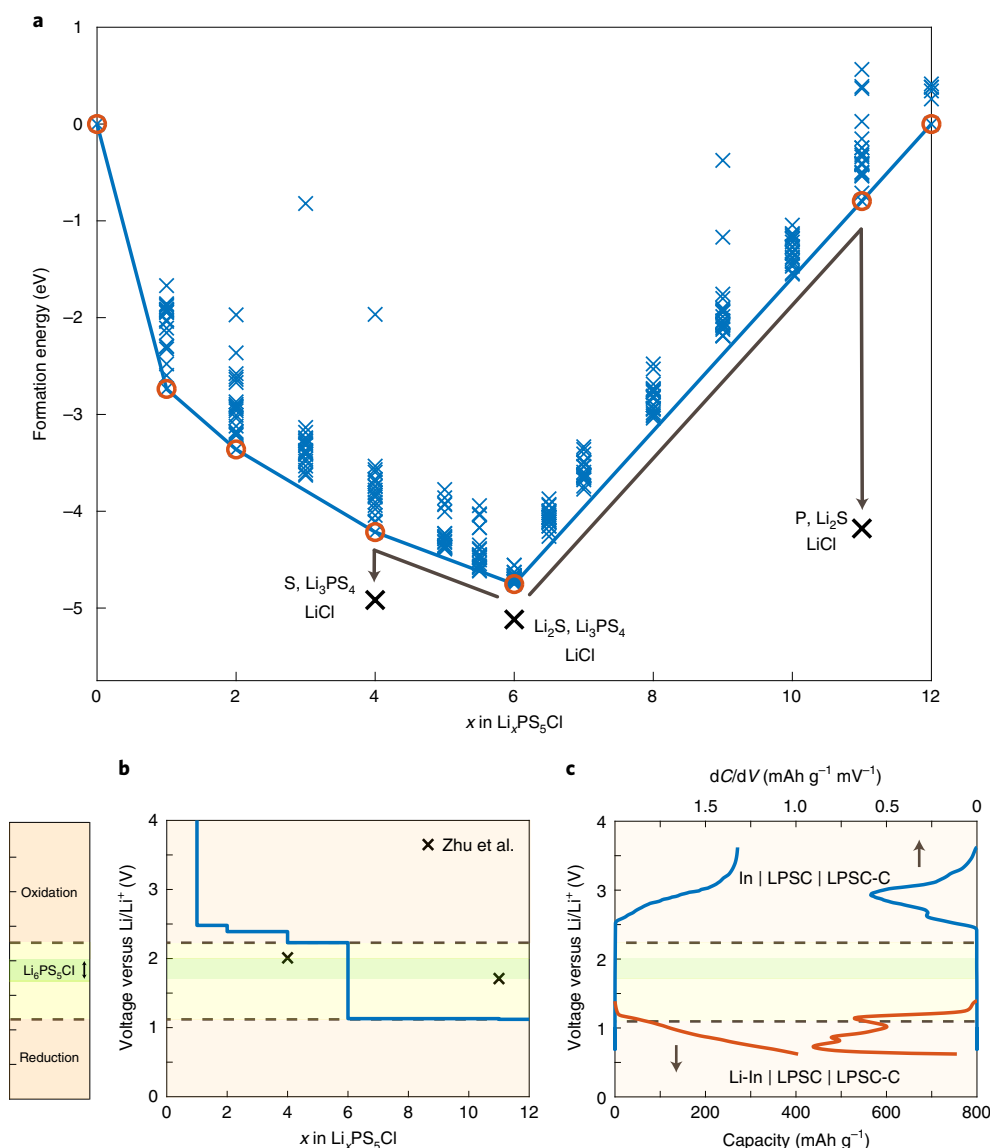


Fig. 2 | Formation energies of Li-vacancy configurations of argyrodite $\text{Li}_x\text{PS}_5\text{Cl}$ and comparison of experimental and calculated voltage profiles.

a, Formation energies per formula unit for all Li configurations within one unit cell versus the composition x in $\text{Li}_x\text{PS}_5\text{Cl}$. The formation energy of the combination of Li_3PS_4 , Li_2S and LiCl is shown below the convex hull at $x=6$. At $x=4$ and $x=11$, the formation energies of the decomposition products on oxidation (S , Li_3PS_4 , LiCl) and on reduction (P , Li_2S and LiCl), respectively, are shown, in line with the decomposition products previously reported¹⁴. **b**, Calculated theoretical voltage profile, versus Li/Li^+ , of $\text{Li}_x\text{PS}_5\text{Cl}$ in the compositional range of $0 < x < 12$. Reduction and oxidation are expected to occur at 1.08 V and 2.24 V versus Li/Li^+ , respectively. The black crosses indicate the voltages at which the argyrodite is expected to decompose, on oxidation to S , Li_3PS_4 , LiCl , and on reduction to P , Li_2S and LiCl , as previously reported¹⁴. **c**, First charge of the $\text{In}|\text{LPSC}|\text{LPSC-C}$ (blue) and first discharge of the $\text{Li-In}|\text{LPSC}|\text{LPSC-C}$ (orange) battery including the differential capacity from Fig. 1d. Above 2.30 V versus Li/Li^+ LPSC is oxidized, and below 1.25 V versus Li/Li^+ LPSC is reduced. The legend compares the stability windows. Yellow region: stability window of LPSC based on the oxidation and reduction potentials of $\text{Li}_4\text{PS}_5\text{Cl}$ and $\text{Li}_{11}\text{PS}_5\text{Cl}$, respectively. Green region: predicted window (thermodynamic), based on the stability of the decomposition products for oxidation (S , Li_3PS_4 , LiCl) and reduction (P , Li_2S and LiCl)^{14,15}.

of the $\text{Li-In}|\text{LPSC}|\text{LPSC}$ battery, shown in Fig. 1d. Indeed, a practical stability window of 1.25 V is obtained, which is much larger than that theoretically predicted (0.3 V)^{14,15} and much smaller than initially reported (7 V)¹⁰. Additionally, the presence of more than one peak, both on reduction and oxidation, indicates subsequent redox activity. This raises the following question: what reactions take place and how do these determine the observed electrochemical stability window?

Aiming for a better understanding and prediction of practical electrochemical stability windows, and correlation with solid electrolyte redox activity, we evaluate the formation energies of

all possible Li-vacancy configurations at different compositions of argyrodite $\text{Li}_x\text{PS}_5\text{Cl}$, within a (charge-neutral) single unit cell, similar to how the energetics of electrode materials are evaluated²⁸. This appears to be a realistic approach considering that the solid electrolyte is in contact with the conductive additives in a cathodic mixture, and therefore the solid electrolyte can function as an electrode material being oxidized and reduced.

The resulting formation energies of the argyrodite $\text{Li}_x\text{PS}_5\text{Cl}$ as a function of Li composition are shown in Fig. 2a, where the convex hull connects the most stable configurations. On oxidation and reduction of LPSC, the most stable compositions are $\text{Li}_4\text{PS}_5\text{Cl}$ and

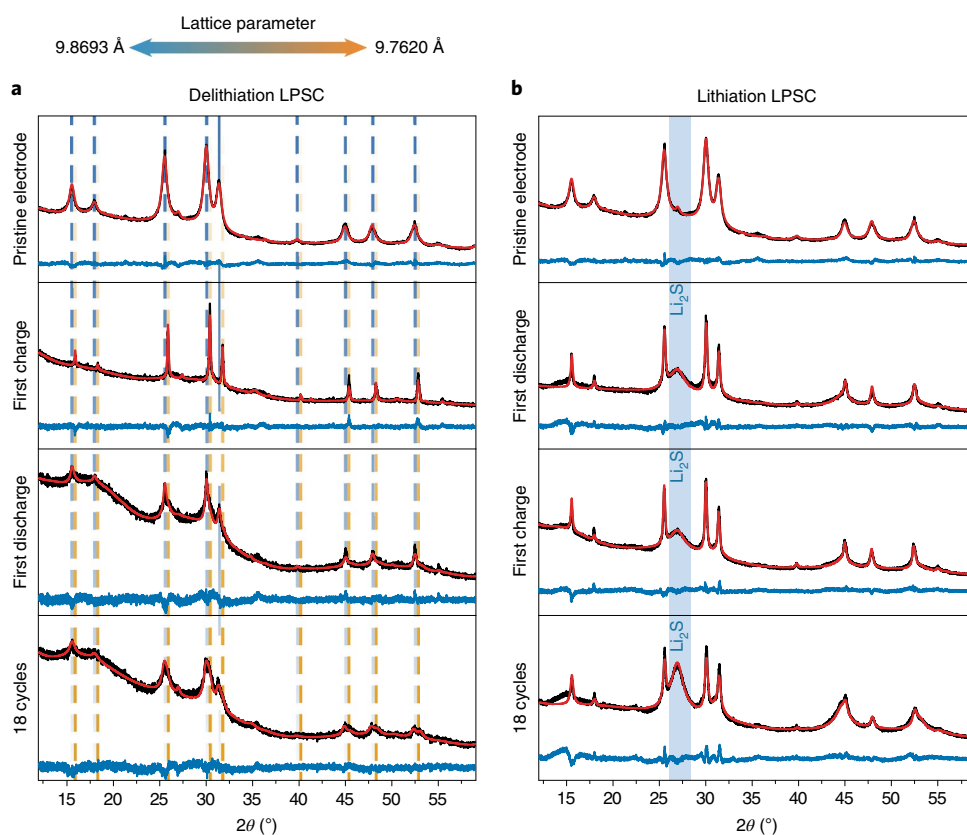


Fig. 3 | XRD patterns and fits of the LPSC-C electrodes before and after cycling. All the patterns are fit with the Rietveld method as implemented in GSAS⁴¹, and the resulting structural parameters are provided in Supplementary Tables 2–7. **a**, XRD patterns for the In|LPSC|LPSC-C battery after first charge to 3.63 V versus Li/Li⁺, after subsequent discharge to 0.63 V versus Li/Li⁺ and after 18 full cycles. **b**, XRD patterns for the Li-In|LPSC|LPSC-C battery after first discharge to 0.63 V versus Li/Li⁺, after subsequent charge to 1.63 V versus Li/Li⁺ and after 18 full cycles. A growing peak at around 27° reflects the formation of the Li₂S phase, which is consistent with the predicted decomposition reaction of lithiated (reduced) argyrodite (Li₁₁PS₅Cl → P + 5 Li₂S + LiCl). The amount of the Li₂S phase that is formed increases dramatically as a function of cycle number, also indicating the continued decomposition of the argyrodite for low potential cycling. After the first half cycle, both on oxidation and reduction, a decrease in peak width is observed, indicating an increase in average crystallite size. The average crystallite size increases from 13 nm to 80 nm on delithiation (**a**) and to 41 nm on lithiation (**b**). An increase in average particle size can be rationalized by the preferential decomposition of smaller particles, most likely due to their large surface areas and resulting shorter electronic pathways for oxidation and reduction. This implies that electronic transport occurs through the argyrodite solid over tens of nanometres (the size of argyrodite particles). On subsequent cycling, the argyrodite XRD peaks widen, which may indicate partial decomposition of larger particles as well as a distribution of argyrodite lattice parameters, as discussed in the main text.

Li₁₁PS₅Cl, respectively. On oxidation of argyrodite, sulfur is redox active (S⁻² → S⁰ + 2e⁻), whereas on reduction, phosphorous is redox active (P⁵⁺ → P⁰ - 5e⁻). Also indicated in Fig. 2a are the energies of the thermodynamically more stable combinations of Li₃PS₄, Li₂S and LiCl species, and the most stable decomposition products of the oxidized and reduced argyrodite. Clearly, a delithiated (oxidized) argyrodite (Li₄PS₅Cl) is much less stable than the combination of Li₃PS₄, S and LiCl, and similarly a lithiated (reduced) argyrodite (Li₁₁PS₅Cl) is much less stable than the combination of P, Li₂S and LiCl, as previously predicted^{14,15}, which are therefore the expected decomposition products on oxidation.

The average voltages as a function of Li composition *x* in Li_{*x*}PS₅Cl, calculated from the convex hull are shown in Fig. 2b. From the theoretical voltage curve it is expected that the argyrodite LPSC delithiates (oxidizes) at 2.24 V and lithiates (reduces) at 1.08 V. This indicates that if the decomposition reactions for oxidation and reduction are determined by the stability of the Li₄PS₅Cl and Li₁₁PS₅Cl species, respectively, an electrochemical stability window of 1.16 V is expected. Also indicated is the much narrower electrochemical stability window, approximately 0.3 V wide, based on direct decomposition into Li₃PS₄, S and LiCl (oxidation) and into

Li₃PS₄, Li₂S and LiCl (reduction), in line with previous DFT calculations^{14,15}. Which stability window applies depends on the activation barriers to these decomposition routes. Based on the high Li-ion conductivity of the argyrodite, indicating low kinetic barriers for changes in the Li composition, we propose that the decomposition occurs indirectly, via the lithiated and delithiated compositions of argyrodite (Li₄PS₅Cl and Li₁₁PS₅Cl), rather than directly into the decomposition products. On argyrodite oxidation and reduction, first Li₄PS₅Cl and Li₁₁PS₅Cl would form, which are most likely unstable as evaluated below, providing a facile reaction pathway towards the formation of the more stable decomposition products as indicated by the solid black arrows in Fig. 2a.

The experimental voltage curves obtained on oxidation and reduction of the argyrodite, including their differential capacity, are shown for comparison in Fig. 2c. Remarkable agreement is found between the predicted electrochemical stability window of 1.16 V (Fig. 2b) and the experimentally observed window (Fig. 2c), supporting the present hypothesis that the argyrodite stability is determined by its redox activity on (de)lithiation. The formation of decomposition products can be expected to increase the impedance depending on their location in the electrodes, which is most likely

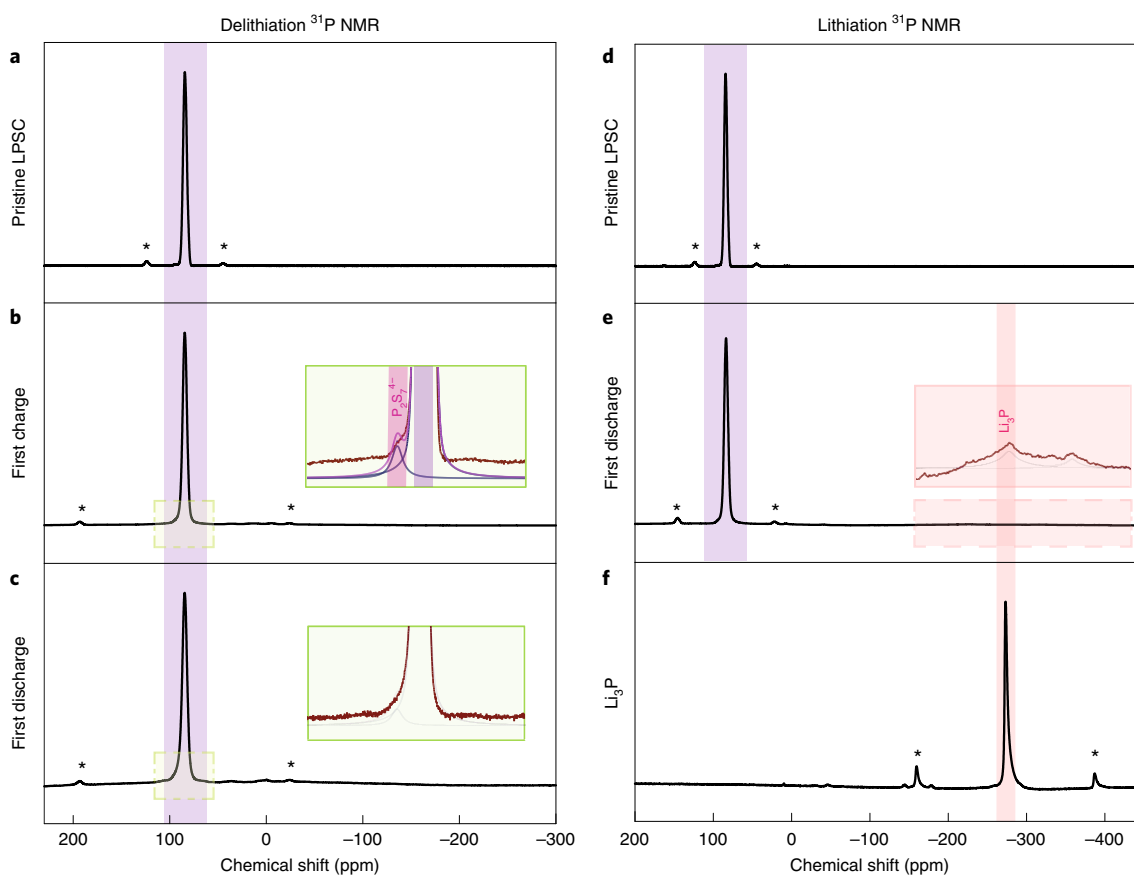


Fig. 4 | Solid-state ^{31}P NMR spectra of pristine, oxidized and reduced LPSC-C. **a–f**, ^{31}P MAS NMR of oxidative (**a–c**) and reductive (**d–f**) activity of LPSC in In|LPSC|LPSC-C and Li-In|LPSC|LPSC-C ASSBs, respectively. Pristine LPSC (**a,d**). After the first charge (**b**), $\text{P}_2\text{S}_7^{4-}$ is found in the cathodic mixture, and after first discharge (**e**), Li_3P is present in the anodic mixture, in agreement with DFT and thermodynamic predictions. Spinning sidebands are indicated with an asterisk.

the origin of the broadening of oxidation and reduction peaks in the differential capacity shown in Fig. 2c. The offset between the measured and predicted stability window is most likely a result of the lower voltages predicted by DFT calculations²⁹. Based on this, we propose that the first oxidation peak in the differential capacity, shown in Fig. 1d and Fig. 2c, is associated with the decomposition of LPSC at around 2.24 V via $\text{Li}_4\text{PS}_5\text{Cl}$ into Li_3PS_4 , S and LiCl, and the first reduction peak in the differential capacity is associated with the decomposition of LPSC at around 1.08 V via $\text{Li}_{11}\text{PS}_5\text{Cl}$ into P, Li_2S and LiCl.

On further oxidation, after the formation of Li_3PS_4 via $\text{Li}_4\text{PS}_5\text{Cl}$, the thermodynamic evaluation predicts the formation of P_2S_5 at 2.3 V (ref. 14). On further reduction, after formation of P via $\text{Li}_{11}\text{PS}_5\text{Cl}$, the thermodynamic evaluation predicts the formation of Li_3P , resulting in several voltage plateaus starting from 1.3 V down to approximately 0.87 V. The latter represents 67% of the reduction capacity (LiP to Li_3P) (see Supplementary Table 1, consistent with previous DFT predictions³⁰). This provides a complete prediction of the oxidation and reduction potential pathway, via the solid electrolyte to the redox activity of the decomposition products as illustrated in Supplementary Fig. 2. For reduction, this is consistent with the observed reduction activity measured at around 0.8 V in Fig. 2c, and with the known reduction potentials associated with the lithiation of phosphorus³¹. However, on oxidation of the expected Li_3PS_4 decomposition product, a peak in the differential capacity is observed around 2.9 V, which is not in agreement with the predicted P_2S_5 formation at 2.3 V. As discussed below, formation of $\text{P}_2\text{S}_7^{4-}$ is

observed, consistent with the P–S–P bridging polyhedral suggested by X-ray photoemission spectroscopy (XPS)²⁰. Moreover, Li_3PS_4 has been observed to oxidize at 2.9 V towards $\text{P}_2\text{S}_7^{4-}$ (ref. 32), consistent with the observed oxidation activity shown in Figs. 1d and 2c. We anticipate that to predict the oxidation of Li_3PS_4 to $\text{P}_2\text{S}_7^{4-}$ at 2.9 V requires a comprehensive DFT redox activity analysis as done here for LPSC.

Additionally, DFT-based molecular dynamics (MD) simulations are performed on the delithiated ($\text{Li}_4\text{PS}_5\text{Cl}$) and lithiated ($\text{Li}_{11}\text{PS}_5\text{Cl}$) phases, showing that the $\text{Li}_4\text{PS}_5\text{Cl}$ and $\text{Li}_{11}\text{PS}_5\text{Cl}$ compositions are extremely unstable, having very low activation barriers towards decomposition (Extended Data Fig. 1). This supports the presently proposed indirect decomposition reaction, through the facile oxidation and reduction of the argyrodite, thus via the unstable $\text{Li}_4\text{PS}_5\text{Cl}$ and $\text{Li}_{11}\text{PS}_5\text{Cl}$ phases, towards the stable decomposition products.

To monitor the structural changes of the LPSC-C electrodes, XRD measurements were performed at different stages during the cycling (following the same cycling strategy as in Fig. 1a,b) of both the In|LPSC|LPSC-C and Li-In|LPSC|LPSC-C batteries as shown in Fig. 3. During the oxidation (delithiation) of the LPSC-C electrode to 3.63 V, the LPSC peak positions shift (Fig. 3a), corresponding to a decrease in the average cubic lattice parameter from 9.87 Å to 9.76 Å. This can be attributed to the partial delithiation of the LPSC phase, consistent with the lattice volume changes predicted by DFT for the compositional range $6 \geq x \geq 4$ for $\text{Li}_x\text{PS}_5\text{Cl}$ (Supplementary Fig. 3). Interestingly, several argyrodite compositions between $\text{Li}_4\text{PS}_5\text{Cl}$ and $\text{Li}_{11}\text{PS}_5\text{Cl}$ are located slightly above the convex hull (only 7.5 meV

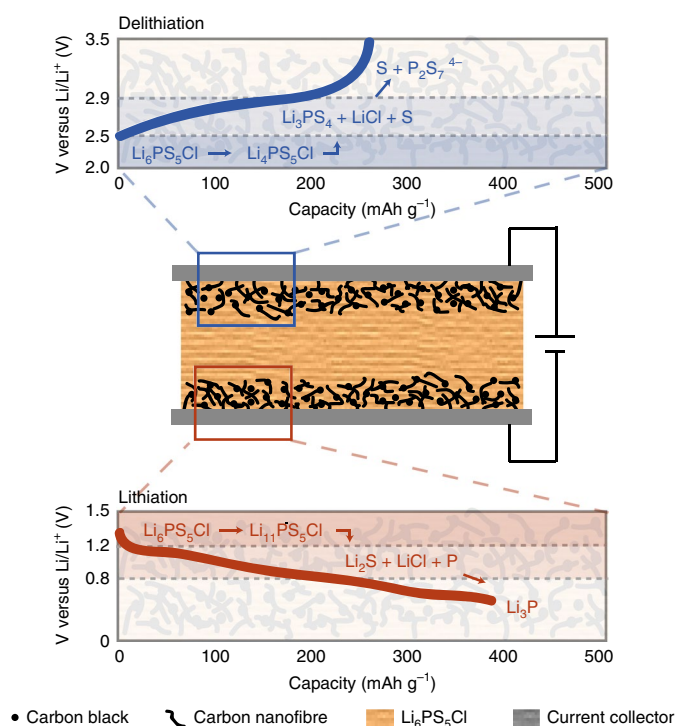


Fig. 5 | Schematic of the electrochemical activity of argyrodite LPSC on oxidation (delithiation) and reduction (lithiation). The electrochemical stability window is determined by the oxidation and reduction potentials of $\text{Li}_4\text{PS}_5\text{Cl}$ (S/S^{2-} redox, at 2.24 V) and $\text{Li}_{11}\text{PS}_5\text{Cl}$ (through the P/P^{5+} redox, at 1.08 V), respectively, here shown schematically, where the activation barriers to form these compositions are expected to be very low based on the high Li-ion conductivity. These redox potentials of the argyrodite solid electrolyte determine the practical electrochemical stability window, as expressed by the first oxidation and reduction reactions observed in the cycling (Fig. 1a,b), and in the differential capacity (Fig. 1d), consistent with the predicted redox activity (Fig. 2). The unstable argyrodite phases rapidly decompose into the expected stable Li_3PS_4 , S and LiCl species after oxidation, and P, Li_2S , and LiCl species after reduction. These decompose on further oxidation and reduction to $\text{P}_2\text{S}_7^{4-}$ and S^0 at 2.9 V (ref. ³²) and Li_3P around 0.8 V (refs. ^{14,15}), respectively, as observed by XPS^{20,21} and the present XRD and NMR analysis. XRD and NMR also demonstrate the presence of metastable (de)lithiated argyrodite phases. This provides strong support for the proposed kinetically most favourable decomposition route, via the redox activity of the argyrodite solid electrolyte, thereby determining the electrochemical stability window.

per atom for $\text{Li}_5\text{PS}_5\text{Cl}$ as seen in Fig. 2a. Based on the convex hull in Fig. 2a, these metastable phases $6 \geq x \geq 4$ should disproportionate into $\text{Li}_4\text{PS}_5\text{Cl}$ (which would decompose immediately) and LPSC. However, in reality, the system will not be in thermodynamic equilibrium as some parts of the electrodes are, or can become, more isolated through poor ionic and/or electronic contact. This makes it reasonable to suggest that parts of the electrode can be captured in $6 \geq x \geq 4$ metastable phases (which are kinetically more stable as compared to the $\text{Li}_4\text{PS}_5\text{Cl}$ and $\text{Li}_{11}\text{PS}_5\text{Cl}$ phases). Importantly, the presence of these phases in the composition range $6 \geq x \geq 4$ provides experimental support for the proposed indirect decomposition mechanism via (de)lithiation of the solid electrolyte. After subsequent reduction, hence after one complete charge–discharge cycle, two different phases of argyrodite appear to be present, indicated by the dashed lines in Fig. 3a. The diffraction angle, 2θ , of the first phase (blue line) shifts back to the pristine argyrodite position, indicating that at least a partially reversible (de)lithiation of LPSC occurs.

The second phase (orange line) remains at the position representing the delithiated argyrodite phases, the amount of which appears to grow on cycling, indicating an increasing amount of oxidized argyrodite phases are formed on cycling. The total amount of crystalline argyrodite decreases as indicated by the increasing background that appears over cycling, indicating the concomitant formation of amorphous sulfide and phosphorous sulfide decomposition products. During the first reduction (lithiation) of the LPSC-C electrode to 0.63 V, the XRD patterns (Fig. 3b) do not display an obvious peak shift, as would be expected for the lithiated phases of argyrodite (Supplementary Fig. 3). A growing peak at around 27° reflects the formation of the Li_2S phase, consistent with the predicted decomposition reaction of lithiated (reduced) argyrodite ($\text{Li}_{11}\text{PS}_5\text{Cl} \rightarrow \text{P} + 5\text{Li}_2\text{S} + \text{LiCl}$). The amount of the Li_2S phase that is formed increases dramatically as a function of cycle number, also indicating the continuous decomposition of the argyrodite for low potential cycling.

Complementary to the XRD measurements, solid-state ^6Li and ^{31}P magic angle spinning (MAS) NMR measurements are performed to analyse the decomposition products formed on cycling. For pristine argyrodite, the ^{31}P resonance at 85 ppm, shown in Fig. 4a,d, can be assigned to the P environment in the PS_4 tetrahedral units³³. After the first oxidation (delithiation) to 3.63 V of the LPSC-C electrode, an additional shoulder is observed at 95 ppm (Fig. 4b), which can be assigned to the ^{31}P environment of $\text{P}_2\text{S}_7^{4-}$ species^{34–36}. This indicates the formation of S–S bonds between PS_4 tetrahedral units (P–S–S–P), which undergoes a disproportionation reaction leading to the formation of $\text{P}_2\text{S}_7^{4-}$ and S^0 , with P–S–P bridging polyhedra²⁰. On first oxidation, the ^6Li NMR spectrum (Extended Data Fig. 2b) shows the formation of an additional shoulder at around -1.1 ppm consistent with the formation of LiCl (ref. ³⁷). This supports the decomposition products observed by XPS^{23,27}, in line with the MD simulations that indicate the bonding of S to PS_4 units. Note that the oxidation to Li_3PS_4 , S and LiCl is proposed at 2.24 V, via the intermediate formation of $\text{Li}_4\text{PS}_5\text{Cl}$, whereas at around 2.9 V the oxidation towards $\text{P}_2\text{S}_7^{4-}$ and S^0 can be expected (Fig. 2b), all due to the S/S^{2-} redox, represented by the first and second oxidation peaks of the differential capacity (Fig. 1d). The line broadening of the ^{31}P and ^6Li resonances of LPSC may originate from a distribution in bond angles and Li-deficient phases observed with XRD (Fig. 3a). After a full cycle that is first oxidation to 3.63 V followed by reduction to 0.63 V, the intensity of the amount of $\text{P}_2\text{S}_7^{4-}$ decreases, whereas in the ^6Li NMR spectrum a new Li environment appears at 0.44 ppm, which can be assigned to Li_3PS_4 (Extended Data Fig. 2c,d). This indicates that the P–S–P bridges connecting the PS_4 units, forming on oxidation, break on reduction transforming them back to isolated PS_4 units, similar to what was reported for the Li_3PS_4 electrolyte^{20,21,38}.

On the first reduction (lithiation) to 0.63 V of the LPSC-C electrode, a new ^{31}P environment appears at -220 ppm (Fig. 4e), which can be assigned to Li_3P (Fig. 4f). The ^6Li NMR spectrum (Extended Data Fig. 2f) shows the appearance of a Li chemical environment very similar to that of Li in the argyrodite. Although the ^6Li chemical shift of this environment is close to that of Li_2PS_3 (Supplementary Fig. 4), the associated phosphorus environment at 109 ppm is not observed in Fig. 4e. We suggest that this Li environment may represent disordered lithiated argyrodite phases, which are suggested to form as metastable phases, occurring just above the convex hull in Fig. 2a. Also, an additional peak appears at 2.3 ppm in the ^6Li spectrum (Extended Data Fig. 2f), which can be assigned to the formation of Li_2S , consistent with the XRD pattern in Fig. 3b. After a full cycle that is first reduction to 0.63 V followed by oxidation to 1.63 V, Li_3P disappears (Supplementary Fig. 5), indicating that in this voltage range phosphorous is redox active, reversibly transforming Li_3PS_4 to Li_3P . The observed formation of Li_3P and Li_2S in the LPSC-C electrodes reduced to 0.63 V is consistent with XPS observations showing the formation of Li_3P , Li_2S and LiCl species at

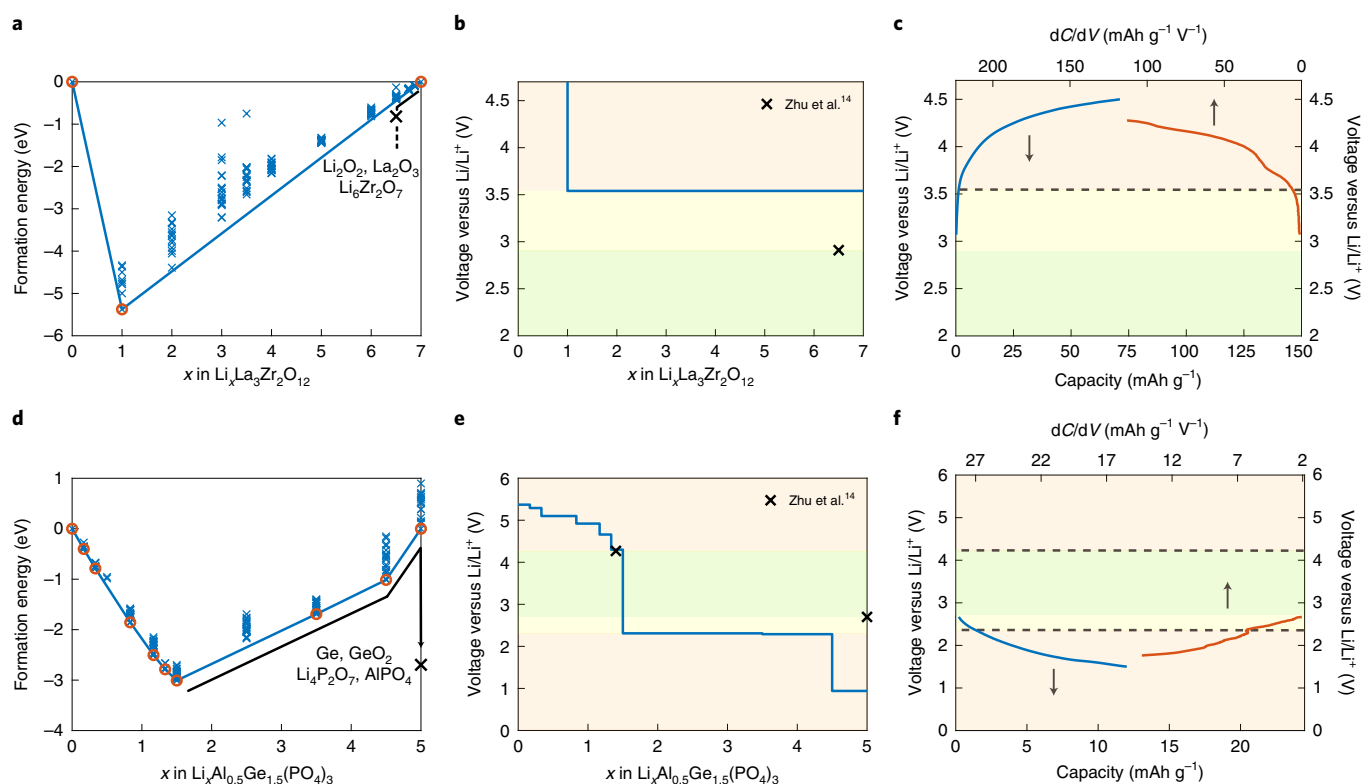


Fig. 6 | Formation energies of Li-vacancy configurations of garnet LLZO and NASICON LAGP solid electrolytes, and comparison of experimental and calculated oxidation potentials. a,d, Formation energies per formula unit of $\text{Li}_x\text{La}_3\text{Zr}_2\text{O}_{12}$ for $0 \leq x \leq 7$ (a) and for $\text{Li}_x\text{Al}_{0.5}\text{Ge}_{1.5}(\text{PO}_4)_3$ $0 \leq x \leq 5$ (d). The formation energies of the decomposition products are indicated with a black cross. It is unlikely that oxidation will proceed to $\text{Li}_x\text{La}_3\text{Zr}_2\text{O}_{12}$ as suggested by the convex hull, because several compositions between $x = 7$ and $x = 6$ (in $\text{Li}_x\text{La}_3\text{Zr}_2\text{O}_{12}$) are located marginally above the convex hull. This suggests that in the presence of slightly higher potentials (>3.54 V), oxidation will lead to indirect decomposition via $x = 6.5$, towards the predicted stable decomposition products Li_2O_2 , La_2O_3 and $\text{Li}_6\text{Zr}_2\text{O}_7$ (ref. ¹⁴). **b,e**, The calculated voltage based on the convex hull of $\text{Li}_x\text{La}_3\text{Zr}_2\text{O}_{12}$ (b) and $\text{Li}_x\text{Al}_{0.5}\text{Ge}_{1.5}(\text{PO}_4)_3$ (e). The blue line represents the redox potentials of the solid electrolytes, and the potentials for direct oxidation/reduction into the decomposition products are indicated with a black cross¹⁴. The green area indicates the stability window assuming direct decomposition, defined by the black cross, and yellow the extended stability window based on the proposed indirect decomposition via (de)lithiation of the solid electrolyte. **c,f** Experimental voltage curve and differential capacity on first oxidation of a Li|liquid electrolyte|LLZO-C battery (c) and first reduction of a Li|liquid electrolyte|LAGP-C battery (f). The differential capacity shows that oxidation of LLZO occurs around 3.6 V and reduction of LAGP occurs around 2.4 V, both in good agreement with the predicted stability window based on the indirect decomposition via (de)lithiation of the solid electrolytes. The specific capacities are calculated based on the weight of LLZO and LAGP respectively. Notably, the reduction of LLZO and the oxidation of LAGP are not considered at present because both the indirect and direct reduction result in practically the same potential, making it impossible to discriminate between the two different mechanisms.

the interface of LPSC with Li metal²². The formation of P, Li_2S and LiCl , through the decomposition of the intermediate $\text{Li}_{11}\text{PS}_5\text{Cl}$, is expected to occur at 1.08 V, and further reduction up to 0.63 V will result in the formation of Li_3P at around 0.8 V (ref. ³¹) as observed (Fig. 1d) and predicted (Fig. 2b).

The proposed indirect oxidative and reductive decomposition mechanism of the argyrodite LPSC solid electrolyte, via the unstable $\text{Li}_4\text{PS}_5\text{Cl}$ (S/S^{2-} redox) and unstable $\text{Li}_{11}\text{PS}_5\text{Cl}$ (P/P^{5+} redox), is schematically shown in Fig. 5. Both the redox activity of the solid electrolyte and of the decomposition products are responsible for the observed cycling capacity at the anodic and cathodic potentials. In ASSBs this implies that both contributions of the solid electrolyte will add to the cycling capacity based on the active electrode materials and the specified potential ranges. Moreover, the poor ionic conductivity of the decomposition products, especially S, Li_2S and LiCl , as well as the change in volume can be expected to be responsible for the large increase in interfacial resistance on cycling^{22,39,40}. In addition to the observed decomposition reactions, specific active materials can result in additional decomposition reactions, for instance Ni_3S_4 on cycling LPSC in combination with a $\text{LiNi}_{0.6}\text{Co}_{0.2}\text{Mn}_{0.2}\text{O}_2$ cathode (Supplementary Fig. 6).

To support the general nature of the indirect decomposition mechanism, the Li insertion/extraction potentials are also determined computationally and experimentally for two different families of solid electrolytes, that is, garnet LLZO and NASICON LAGP, as shown in Fig. 6. For LLZO, the predicted and measured oxidation are both located just above 3.5 V, which is significantly larger than the direct decomposition at 2.91 V towards the predicted stable decomposition products Li_2O_2 , La_2O_3 and $\text{Li}_6\text{Zr}_2\text{O}_7$ (ref. ¹⁴). For LAGP, the predicted and measured oxidation occur close to 2.31 V, which is lower than direct decomposition at 2.70 V based on the stability of the predicted decomposition products Ge, GeO_2 , $\text{Li}_4\text{P}_2\text{O}_7$ and AlPO_4 (ref. ¹⁴). These results support the hypothesis that the proposed indirect, kinetically favourable decomposition, via the (de)lithiation of the solid electrolyte, is a general mechanism, in practice widening the solid electrolyte stability window.

As solid electrolytes are designed for high ionic conductivity, the activation energies for oxidation and reduction reactions, associated with delithiation and lithiation respectively, can be expected to be small. The resulting metastable solid electrolyte compositions provide a kinetically facile reaction intermediate, providing an indirect pathway towards the more stable solid electrolyte

decomposition products. As a consequence, the electrochemical stability window is determined by the solid electrolyte oxidation and reduction potentials (S and P redox for argyrodite and several other thiophosphate based solid electrolytes, O and Zr redox for LLZO and O and P redox for LAGP), and not by the stability of the most stable solid electrolyte decomposition products. The consequence of this indirect thermodynamic pathway is that the electrochemical stability window is generally wider than that based on only the stability of the decomposition products. Based on this mechanism, the design of stable solid electrolytes and their interfaces should focus on maximizing the (de)lithiation redox potentials of the solid electrolytes. The demonstrated relation between the solid electrolyte electrochemical stability window and the redox reactions of the electrolyte are decisive for the performance of solid-state batteries and provide understanding that will contribute to the design of electrolyte–electrode interfaces in ASSBs.

Online content

Any methods, additional references, Nature Research reporting summaries, source data, extended data, supplementary information, acknowledgements, peer review information; details of author contributions and competing interests; and statements of data and code availability are available at <https://doi.org/10.1038/s41563-019-0576-0>.

Received: 3 June 2019; Accepted: 28 November 2019;

Published online: 13 January 2020

References

- Kim, J. G. et al. A review of lithium and non-lithium based solid state batteries. *J. Power Sources* **282**, 299–322 (2015).
- Zhang, Z. et al. New horizons for inorganic solid state ion conductors. *Energy Environ. Sci.* **11**, 1945–1976 (2018).
- Janek, J. & Zeier, W. G. A solid future for battery development. *Nat. Energy* **1**, 16141 (2016).
- Zheng, F., Kotobuki, M., Song, S., Lai, M. O. & Lu, L. Review on solid electrolytes for all-solid-state lithium-ion batteries. *J. Power Sources* **389**, 198–213 (2018).
- Fergus, J. W. Ceramic and polymeric solid electrolytes for lithium-ion batteries. *J. Power Sources* **195**, 4554–4569 (2010).
- Yu, C., van Eijck, L., Ganapathy, S. & Wagemaker, M. Synthesis, structure and electrochemical performance of the argyrodite $\text{Li}_4\text{PS}_2\text{Cl}$ solid electrolyte for Li-ion solid state batteries. *Electrochim. Acta* **215**, 93–99 (2016).
- Famprikis, T., Canepa, P., Dawson, J. A., Islam, M. S. & Masquelier, C. Fundamentals of inorganic solid-state electrolytes for batteries. *Nat. Mater.* **18**, 1278–1291 (2019).
- Kamaya, N. et al. A lithium superionic conductor. *Nat. Mater.* **10**, 682–686 (2011).
- Ohta, S., Kobayashi, T. & Asaoka, T. High lithium ionic conductivity in the garnet-type oxide $\text{Li}_{7-x}\text{La}_3(\text{Zr}_{2-x}\text{Nb}_x)\text{O}_{12}$ ($x = 0-2$). *J. Power Sources* **196**, 3342–3345 (2011).
- Boulineau, S., Courty, M., Tarascon, J.-M. & Viallet, V. Mechanochemical synthesis of Li-argyrodite $\text{Li}_4\text{PS}_2\text{X}$ ($X = \text{Cl}, \text{Br}, \text{I}$) as sulfur-based solid electrolytes for all solid state batteries application. *Solid State Ion.* **221**, 1–5 (2012).
- Kato, Y. et al. High-power all-solid-state batteries using sulfide superionic conductors. *Nat. Energy* **1**, 16030 (2016).
- Lotsch, B. V. & Maier, J. Relevance of solid electrolytes for lithium-based batteries: a realistic view. *J. Electroceram.* **38**, 128–141 (2017).
- Tian, Y. et al. Compatibility issues between electrodes and electrolytes in solid-state batteries. *Energy Environ. Sci.* **10**, 1150–1166 (2017).
- Zhu, Y., He, X. & Mo, Y. Origin of outstanding stability in the lithium solid electrolyte materials: insights from thermodynamic analyses based on first-principles calculations. *ACS Appl. Mater. Interfaces* **7**, 23685–23693 (2015).
- Richards, W. D., Miara, L. J., Wang, Y., Kim, J. C. & Ceder, G. Interface stability in solid-state batteries. *Chem. Mater.* **28**, 266–273 (2016).
- Han, F., Gao, T., Zhu, Y., Gaskell, K. J. & Wang, C. A battery made from a single material. *Adv. Mater.* **27**, 3473–3483 (2015).
- Zhang, W. et al. The detrimental effects of carbon additives in $\text{Li}_{10}\text{GeP}_2\text{S}_{12}$ -based solid-state batteries. *ACS Appl. Mater. Interfaces* **9**, 35888–35896 (2017).
- Han, F. et al. High electronic conductivity as the origin of lithium dendrite formation within solid electrolytes. *Nat. Energy* **4**, 187–196 (2019).
- Han, F., Zhu, Y., He, X., Mo, Y. & Wang, C. Electrochemical stability of $\text{Li}_{10}\text{GeP}_2\text{S}_{12}$ and $\text{Li}_7\text{La}_3\text{Zr}_2\text{O}_{12}$ solid electrolytes. *Adv. Energy Mater.* **6**, 1501590 (2016).
- Koerver, R. et al. Redox-active cathode interphases in solid-state batteries. *J. Mater. Chem. A* **5**, 22750–22760 (2017).
- Hakari, T. et al. Structural and electronic-state changes of a sulfide solid electrolyte during the Li deinsertion–insertion processes. *Chem. Mater.* **29**, 4768–4774 (2017).
- Wenzel, S., Sedmaier, S. J., Dietrich, C., Zeier, W. G. & Janek, J. Interfacial reactivity and interphase growth of argyrodite solid electrolytes at lithium metal electrodes. *Solid State Ion.* **318**, 102–112 (2018).
- Auvergniot, J. et al. Interface stability of argyrodite $\text{Li}_4\text{PS}_2\text{Cl}$ toward LiCoO_2 , $\text{LiNi}_{1/3}\text{Co}_{1/3}\text{Mn}_{1/3}\text{O}_2$, and LiMn_2O_4 in bulk all-solid-state batteries. *Chem. Mater.* **29**, 3883–3890 (2017).
- Lau, J. et al. Sulfide solid electrolytes for lithium battery applications. *Adv. Energy Mater.* **8**, 1800933 (2018).
- Tan, D. H. S. et al. Elucidating reversible electrochemical redox of $\text{Li}_4\text{PS}_2\text{Cl}$ solid electrolyte. *ACS Energy Lett.* **4**, 2418–2427 (2019).
- Deiseroth, H.-J. et al. $\text{Li}_4\text{PS}_2\text{X}$: a class of crystalline Li-rich solids with an unusually high Li^+ mobility. *Angew. Chem.* **47**, 755–758 (2008).
- Auvergniot, J. et al. Redox activity of argyrodite $\text{Li}_4\text{PS}_2\text{Cl}$ electrolyte in all-solid-state Li-ion battery: an XPS study. *Solid State Ion.* **300**, 78–85 (2017).
- Aydinol, M. K., Kohan, A. F. & Ceder, G. Ab initio calculation of the intercalation voltage of lithium-transition-metal oxide electrodes for rechargeable batteries. *J. Power Sources* **68**, 664–668 (1997).
- Aydinol, M. K., Kohan, A. F., Ceder, G., Cho, K. & Joannopoulos, J. Ab initio study of lithium intercalation in metal oxides and metal dichalcogenides. *Phys. Rev. B* **56**, 1354–1365 (1997).
- Mayo, M., Griffith, K. J., Pickard, C. J. & Morris, A. J. Ab initio study of phosphorus anodes for lithium- and sodium-ion batteries. *Chem. Mater.* **28**, 2011–2021 (2016).
- Ramireddy, T. et al. Phosphorus–carbon nanocomposite anodes for lithium-ion and sodium-ion batteries. *J. Mater. Chem. A* **3**, 5572–5584 (2015).
- Hakari, T., Nagao, M., Hayashi, A. & Tatsumisago, M. All-solid-state lithium batteries with Li_4PS_4 glass as active material. *J. Power Sources* **293**, 721–725 (2015).
- Deiseroth, H. J. et al. $\text{Li}_4\text{PS}_2\text{X}$: a class of crystalline Li-rich solids with an unusually high Li^+ mobility. *Angew. Chem. Int. Ed.* **47**, 755–758 (2008).
- Dietrich, C. et al. Local structural investigations, defect formation, and ionic conductivity of the lithium ionic conductor $\text{Li}_4\text{P}_2\text{S}_6$. *Chem. Mater.* **28**, 8764–8773 (2016).
- Dietrich, C. et al. Lithium ion conductivity in Li_2S – P_2S_5 glasses—building units and local structure evolution during the crystallization of superionic conductors Li_3PS_4 , $\text{Li}_7\text{P}_3\text{S}_{11}$ and $\text{Li}_4\text{P}_2\text{S}_7$. *J. Mater. Chem. A* **5**, 18111–18119 (2017).
- Murakami, M. et al. Dynamical origin of ionic conductivity for $\text{Li}_7\text{P}_3\text{S}_{11}$ metastable crystal as studied by ^6Li and ^{31}P solid-state NMR. *J. Phys. Chem. C* **119**, 24248–24254 (2015).
- Meyer, B. M., Leifer, N., Sakamoto, S., Greenbaum, S. G. & Grey, C. P. High field multinuclear NMR investigation of the SEI layer in lithium rechargeable batteries. *Electrochem. Solid State Lett.* **8**, A145–A148 (2005).
- Stöfler, H. et al. Amorphous versus crystalline Li_3PS_4 : local structural changes during synthesis and Li ion mobility. *J. Phys. Chem. C* **123**, 10280–10290 (2019).
- Yu, C. et al. Accessing the bottleneck in all-solid state batteries, lithium-ion transport over the solid-electrolyte-electrode interface. *Nat. Commun.* **8**, 1086 (2017).
- Zhang, W. et al. (Electro)chemical expansion during cycling: monitoring the pressure changes in operating solid-state lithium batteries. *J. Mater. Chem. A* **5**, 9929–9936 (2017).
- Larson, A. C. & Von Dreele, R. B. *General Structure Analysis System (GSAS)* (Los Alamos National Laboratory, 2004).

Publisher's note Springer Nature remains neutral with regard to jurisdictional claims in published maps and institutional affiliations.

© The Author(s), under exclusive licence to Springer Nature Limited 2020

Methods

Synthesis. Argyrodite LPSC was synthesized as described in detail previously⁴². Appropriate amounts of Li₂S (99.9%, Alfa Aesar), P₂S₅ (99%, Sigma-Aldrich) and LiCl (99.0%, Sigma-Aldrich) were ball milled at 110 r.p.m. for 2 h under argon atmosphere. The mixture was then transferred to quartz tubes and annealed at 550 °C for 15 h to get the pure phase of the argyrodite LPSC (Supplementary Fig. 7).

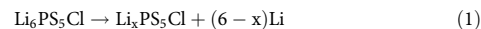
Solid-state battery assembly and electrochemical cycling. The electrode mixture was prepared by ball milling argyrodite with carbon (Super P, TIMCAL) and carbon nanofibres (Sigma-Aldrich) in a weight ratio of 0.70:0.15:0.15 for 6 h at 450 r.p.m. in a ZrO₂-coated stainless steel jar with eight ZrO₂ balls. The solid electrolyte and electrodes were then cold pressed under 5 tonne cm⁻² in a solid-state cell. In a cell, 10 mg of LPSC-C electrode was used and pressed against 180 mg of electrolyte^{42,43}. Cycling was performed in an argon-filled glove box, to avoid reactions with oxygen and moisture. The ASSBs were cycled galvanostatically with a current density of 5.5 mA cm⁻² within a voltage window of 0–3 V versus In for In|LPSC|LPSC-C, 0–1 V versus Li/In for Li-In|LPSC|LPSC-C and 0–2.5 V for LPSC-C|LPSC|LPSC-C. To evaluate the practical electrochemical stability window more accurately, the differential capacity was determined from the first charge of the In|LPSC|LPSC-C battery and from the first discharge of the Li-In|LPSC|LPSC-C battery. Often cyclic voltammetry is used to determine the experimental stability window. However, the relatively short exposure time to the decomposition potentials in combination with the typically sluggish decomposition reactions make it challenging to evaluate the electrochemical stability window with cyclic voltammetry. In contrast, the differential capacity, determined from the slow galvanostatic charge and discharge profiles of individual oxidation and reduction processes, is effective in determining the practical electrochemical stability window, particularly when the solid electrolyte is used as an active electrode material. To measure the oxidative and reductive stability of LLZO and LAGP, an N-Methyl-2-pyrrolidone (Sigma-Aldrich) based electrode slurry was prepared by ball milling active material (LLZO Ta-doped, of 400–600 nm, Ampcera; LAGP, Ampcera), with carbon black (Super P, TIMCAL), PVDF (polyvinylidene fluoride) binder (Solef PVDF, Solvay) in the weight ratio 0.4:0.5:0.1 for 90 min at 250 r.p.m. in a ZrO₂-coated stainless steel jar with eight ZrO₂ balls. A blank test was prepared using carbon black (Super P, TIMCAL) as active material and PVDF as a binder in the weight ratio 0.9:0.1 to result in the same carbon black loading as the LLZO and LAGP electrodes. The slurry was cast on Al foil with a thickness of 100 μm and dried at 60 °C in a vacuum oven for 12 h. The loading of the LLZO, LAGP and carbon electrodes was 1.6, 1.0 and 0.6 mg cm⁻², respectively. The coin cells were assembled in an argon-filled glove box, to avoid reactions with oxygen and moisture (<0.1 ppm O₂ and <2 ppm H₂O) using both a polymer (Celgard 2250) and a glass fibre (Whatman) separator, and lithium metal as a counter electrode (Sigma-Aldrich), which is washed with dimethyl carbonate to remove the oxide layer. 400 μl of 1.0 M LiPF₆ in 1:1 v/v ethylene carbonate and diethyl carbonate (<15 ppm H₂O, Sigma-Aldrich) was added as an electrolyte for wetting both working and counter electrode surfaces. Galvanostatic oxidation was performed with a cut-off voltage of 4.5 V (versus Li/Li⁺) for first oxidation (LLZO-C) and 1.5 V (versus Li/Li⁺) for first reduction (LAGP-C), with 12 h of rest, and a charge–discharge current of 7.0 μA. Comparison of the galvanostatic oxidation and reduction of the LLZO-C and LAGP-C electrodes and a blank electrode are provided in Supplementary Fig. 8a,b. With the solid electrolyte–carbon mixtures, very large interface areas were achieved (for the current particle sizes of »1 m²) making the effective current densities at least four orders of magnitude lower than the current densities based on the electrode diameter.

X-ray diffraction. To identify the crystalline phases of the prepared materials, powder XRD patterns were collected in the 2θ range of 10–120° using Cu Kα X-rays (1.5406 Å at 45 kV and 40 mA) on an X'Pert Pro X-ray diffractometer (PANalytical). The samples were tested in an airtight sample holder, filled with argon, to prevent exposure to oxygen and moisture.

Solid-state NMR. Solid-state NMR measurements were performed using a Bruker Ascend 500 MHz spectrometer equipped with two- and three-channel 4.0 mm and 3.2 mm MAS probes, respectively. The operating frequencies for ³¹P and ⁶Li were 202.47 and 73.60 MHz, respectively, and all measurements were performed within a spinning speed range of 8–23 kHz and π/2 pulse lengths of 4–5 μs were determined for ⁶Li and ³¹P. The chemical shifts of ⁶Li spectra were referenced with respect to a 0.1 M LiCl solution, and those of ³¹P spectra with respect to an 85% H₃PO₄ solution. Based on the spin-lattice (T₁) relaxation time, recycle delays of 5–10,000 s were used, collecting between 128 and 11,264 scans for each sample.

Computational details. Argyrodite Li₆PS₅Cl crystallizes in the F43m space group and at x = 6 has 50% of the 48-h crystallographic Li positions randomly occupied⁶. The starting structure of the argyrodite was obtained from the literature, where a thorough investigation of the most stable configuration was performed, taking into account the halogen disorder⁴⁴. By calculating the energies of the non-equivalent Li configurations, the most stable Li₆PS₅Cl configurations were obtained, from which the voltage at which these phases were formed can be determined.

To determine the energy properties of the crystalline phases, DFT relaxations were performed with the Vienna Ab initio Simulation Package (VASP)⁴⁵. The Perdew, Burke and Ernzerhof (PBE) exchange correlation functional of Perdew et al. was implemented⁴⁶, and core electrons were probed with the projected-augmented wave approach⁴⁷. A cut-off value of 280 eV and a 4 × 4 × 4 k-point mesh were used. For the argyrodite, the following reaction is considered:



If $x < 6$, Li LPSC is oxidized; if $x > 6$ LPSC is reduced. Then, by calculating the energies on both sides of the reaction and taking the electrochemical potential of Li into account,

$$\bar{\mu}_{\text{Li}} = \mu_{\text{Li}} - \phi \quad (2)$$

with $\bar{\mu}_{\text{Li}}$ the electrochemical potential of Li, μ_{Li} the chemical potential of Li and ϕ the electrical potential. Therefore, the average electrical potential at which oxidation/reduction takes place can be determined by

$$\bar{\phi} = -\frac{E(\text{Li}_6\text{PS}_5\text{Cl}) - E(\text{Li}_x\text{PS}_5\text{Cl}) - (6-x)E(\text{Li})}{6-x} \quad (3)$$

where $E(\text{Li}_x\text{PS}_5\text{Cl})$ represents the composition of the most stable configurations on the convex hull. DFT-based MD simulations were performed using the same cut-off value as in DFT simulations. The ab initio MD simulations were executed in the NVT ensemble (conserving the number of atoms, volume and temperature), where the temperature scales every 1,000 time steps. The simulations use periodic boundary conditions with time steps of 2 fs, the total time of the MD simulations being 100 ps. The number of k-points was reduced from 4 × 4 × 4 used in the DFT simulations to 1 × 1 × 1 for the MD simulations. The lattice parameters and positions of all atoms were allowed to relax during relaxation.

The argyrodite structure was obtained from previous work⁴⁴. There the Cl–S disorder over the 4a and 4c sites was investigated, and the thermodynamically most favourable configuration was obtained. Note that the Cl–S disorder was kept constant in the presented convex hull and thus the oxidation and reduction voltages were not affected. For determination of configurations as a function of the Li concentration, 10,000 structures were created by placing the appropriate number of Li ions randomly at the 48-h positions. To quickly scan these for possible low-energy structures, only the electrostatic energies in these structures were calculated, using the undamped shifted force method with a cut-off radius of 15 Å (ref. 48). For the 20 lowest energy configurations of the electrostatic calculations the structure was optimized and the energy was calculated using VASP. For Li_xPS₅Cl, 12 ≤ x ≤ 15, extra Li atoms were inserted on the 16e position, and the extended convex hull is presented in Supplementary Fig. 9.

All DFT calculations were performed on charge-neutral cells, thus taking into account the true oxidation and reduction of solid electrolytes, and thus behaving similar to an electrode material. The formation energies of the thermodynamic decomposition products were taken from the Materials Project database⁴⁹. The structure of LLZO was also obtained from the Materials Project database⁴⁹. For LLZO, a 1 × 1 × 1 k-point mesh was used with a cut-off value of 500 eV. The structure of LAGP was taken from the literature⁵⁰ and was relaxed using a 3 × 3 × 1 k-point mesh with a cut-off value of 500 eV.

Data availability

The datasets generated during and/or analysed during the current study are available from the corresponding authors on reasonable request.

References

- Yu, C. et al. Facile synthesis toward the optimal structure-conductivity characteristics of the argyrodite Li₆PS₅Cl solid-state electrolyte. *ACS Appl. Mater. Interfaces* **10**, 33296–33306 (2018).
- Yu, C. et al. Tailoring Li₆PS₅Br ionic conductivity and understanding of its role in cathode mixtures for high performance all-solid-state Li–S batteries. *J. Mater. Chem. A* **7**, 10412–10421 (2019).
- de Klerk, N. J. J., Rosloň, I. & Wagemaker, M. Diffusion mechanism of Li argyrodite solid electrolytes for Li-ion batteries and prediction of optimized halogen doping: the effect of Li vacancies, halogens, and halogen disorder. *Chem. Mater.* **28**, 7955–7963 (2016).
- Kresse, G. & Hafner, J. Ab initio molecular dynamics for liquid metals. *Phys. Rev. B* **47**, 558–561 (1993).
- Perdew, J. P., Burke, K. & Wang, Y. Generalized gradient approximation for the exchange-correlation hole of a many-electron system. *Phys. Rev. B* **54**, 16533–16539 (1996).
- Blöchl, P. E. Projector augmented-wave method. *Phys. Rev. B* **50**, 17953–17979 (1994).
- Fennell, C. J. & Gezelter, J. D. Is the Ewald summation still necessary? Pairwise alternatives to the accepted standard for long-range electrostatics. *J. Chem. Phys.* **124**, 234104 (2006).
- Jain, A. et al. The Materials Project: a materials genome approach to accelerating materials innovation. *APL Mater.* **1**, 011002 (2013).

50. Kang, J., Chung, H., Doh, C., Kang, B. & Han, B. Integrated study of first principles calculations and experimental measurements for Li-ionic conductivity in Al-doped solid-state $\text{LiGe}_2(\text{PO}_4)_3$ electrolyte. *J. Power Sources* **293**, 11–16 (2015).

Acknowledgements

The authors thank K. Goubitz, M. Steenvoorden and F. Ooms for their assistance with experiments and C. Robledo for her assistance with the schematic graphic. Financial support is acknowledged from the Netherlands Organization for Scientific Research (NWO) under the VICI grant no. 16122, from the eScience Centre and NWO under the joint CSER and eScience programme for Energy Research grant no. 680.91.087 and from the Advanced Dutch Energy Materials (ADEM) programme of the Dutch Ministry of Economic Affairs, Agriculture and Innovation.

Author contributions

T.S., A.V. and N.J.J.d.K. carried out the DFT simulations and T.S. and A.V. analysed the data. C.Y. and C.W. synthesized the solid electrolytes. T.S., C.W., V.A. carried out

the electrochemical measurements and T.S. and V.A. analysed the data. T.S., V.A. and C.W. carried out the XRD measurements and V.A., T.S. and S.G. analysed the data. V.A. measured and analysed the NMR data. C.Y., E.v.d.M., Y.X. and J.H. carried out preliminary measurements. T.H., I.K. and E.M.K. contributed to the discussion of results. M.W. supervised the project. S.G. and M.W. designed the research. T.S., V.A., S.G. and M.W. wrote the manuscript.

Competing interests

The authors declare no competing interests.

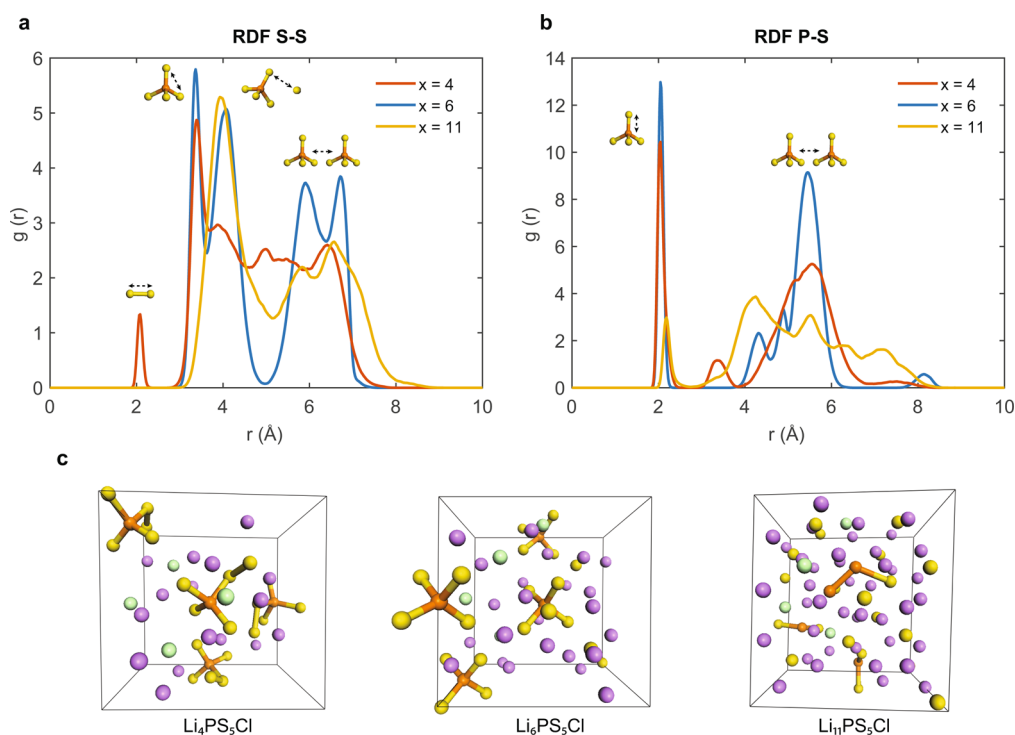
Additional information

Extended data is available for this paper at <https://doi.org/10.1038/s41563-019-0576-0>.

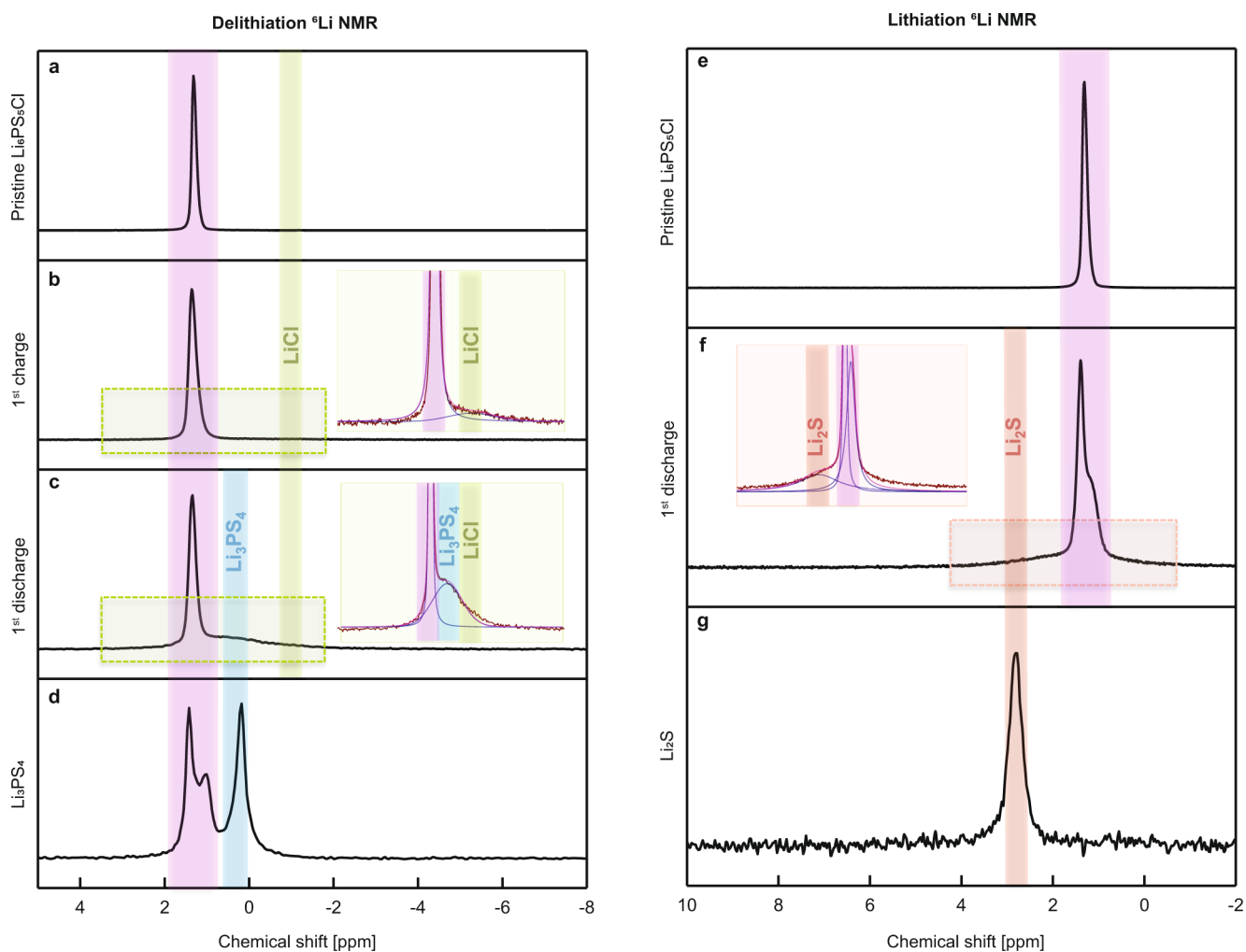
Supplementary information is available for this paper at <https://doi.org/10.1038/s41563-019-0576-0>.

Correspondence and requests for materials should be addressed to S.G. or M.W.

Reprints and permissions information is available at www.nature.com/reprints.



Extended Data Fig. 1 | Molecular dynamics simulations of $\text{Li}_4\text{PS}_5\text{Cl}$, $\text{Li}_6\text{PS}_5\text{Cl}$ and $\text{Li}_{11}\text{PS}_5\text{Cl}$. **a**, Radial distribution function (RDF) of the S-S bonds in (de)lithiated $\text{Li}_x\text{PS}_5\text{Cl}$ for $x = 4, 6$, and 11 during a 400 K DFT-MD simulation. During delithiation an increase in S-S bonds is seen around 2.1 \AA , indicating that the formation of S-S bonds originates from the oxidation of S in the argyrodite. On top of the peaks, bonds at corresponding radii are displayed. It is important to realize that the timescale at which these structural transformations can be evaluated is very limited and therefore sluggish transformations fall outside the scope of this evaluation. **b**, Radial distribution function (RDF) of the P-S bonds of (de)lithiated $\text{Li}_x\text{PS}_5\text{Cl}$ for $x = 4, 6$ and 11 during a 400 K DFT-MD simulation. For the lithiated phase, $\text{Li}_{11}\text{PS}_5\text{Cl}$, a drop in intensity is observed at $r = 2.1\text{ \AA}$, consistent with breaking P-S bonds in the PS_4 groups. This is expected because the P atoms can compensate for the change in valence as a consequence of the lithiation. The MD simulations indicate that the $\text{Li}_4\text{PS}_5\text{Cl}$ and $\text{Li}_{11}\text{PS}_5\text{Cl}$ compositions are extremely unstable, having very low activation barriers towards decomposition. Their instability suggests that these compositions will only occur locally in the material, rapidly initiating local decomposition, which will nevertheless require the associated oxidation or reduction potential predicted by the convex hull shown in Fig. 2b. **c**, Relaxed structures of $\text{Li}_x\text{PS}_5\text{Cl}$ for $x = 4, 6$ and 11 after a 400 K DFT-MD simulation. The violet, orange, yellow and green spheres indicate lithium, phosphorous, sulfur, and chlorine respectively.



Extended Data Fig. 2 | ^6Li MAS NMR spectra of the cathodic mixtures and anodic mixtures. ^6Li MAS NMR spectra of the cathodic mixtures (a–d) and anodic mixtures (e–g) of $\text{Li}_6\text{PS}_5\text{Cl}$ in the In|LPSC|LPSC-C and Li-In|LPSC|LPSC-C solid-state batteries respectively. After first charge of the In|LPSC|LPSC-C solid-state cell, formation of LiCl is observed (b). First discharge shows formation at a new resonance frequency corresponding to Li_3PS_4 (c, d). The solid state cell, which starts from lithiation process (f), results in formation of Li_2S , confirmed with the spectrum of the reference Li_2S (g).